CFHTLenS: Testing the Laws of Gravity with Tomographic Weak Lensing and Redshift Space Distortions

Fergus Simpson[1]⋆, Catherine Heymans[1], David Parkinson[2], Chris Blake[3],
Martin Kilbinger[4,5,6], Jonathan Benjamin[7], Thomas Erben[8], Hendrik Hildebrandt[7,8],
Henk Hoekstra[9,10], Thomas D. Kitching[1], Yannick Mellier[11], Lance Miller[12],
Ludovic Van Waerbeke[7], Jean Coupon[13], Liping Fu[14], Joachim Harnois-Déraps[15,16],
Michael J. Hudson[17,18], Konrad Kuijken[9], Barnaby Rowe[19,20], Tim Schrabback[8,9,21],
Elisabetta Semboloni[9], Sanaz Vafaei[7], Malin Velander[12,9].

[1]*Scottish Universities Physics Alliance, Institute for Astronomy, University of Edinburgh, Royal Observatory, Blackford Hill, Edinburgh, EH9 3HJ, UK.*
[2]*School of Mathematics and Physics, University of Queensland, Brisbane, QLD 4072, Australia*
[3]*Centre for Astrophysics & Supercomputing, Swinburne University of Technology, P.O. Box 218, Hawthorn, VIC 3122, Australia*
[4]*CEA Saclay, Service d'Astrophysique (SAp), Orme des Merisiers, Bât 709, F-91191 Gif-sur-Yvette, France.*
[5]*Excellence Cluster Universe, Boltzmannstr. 2, D-85748 Garching, Germany.*
[6]*Universitäts-Sternwarte, Ludwig-Maximillians-Universität München, Scheinerstr. 1, 81679 München, Germany.*
[7]*Department of Physics and Astronomy, University of British Columbia, 6224 Agricultural Road, Vancouver, V6T 1Z1, BC, Canada.*
[8]*Argelander Institute for Astronomy, University of Bonn, Auf dem Hügel 71, 53121 Bonn, Germany.*
[9]*Leiden Observatory, Leiden University, Niels Bohrweg 2, 2333 CA Leiden, The Netherlands.*
[10]*Department of Physics and Astronomy, University of Victoria, Victoria, BC V8P 5C2, Canada.*
[11]*Institut d'Astrophysique de Paris, Université Pierre et Marie Curie - Paris 6, 98 bis Boulevard Arago, F-75014 Paris, France.*
[12]*Department of Physics, Oxford University, Keble Road, Oxford OX1 3RH, UK.*
[13]*Institute of Astronomy and Astrophysics, Academia Sinica, P.O. Box 23-141, Taipei 10617, Taiwan.*
[14]*Key Lab for Astrophysics, Shanghai Normal University, 100 Guilin Road, 200234, Shanghai, China.*
[15]*Canadian Institute for Theoretical Astrophysics, University of Toronto, M5S 3H8, Ontario, Canada.*
[16]*Department of Physics, University of Toronto, M5S 1A7, Ontario, Canada.*
[17]*Department of Physics and Astronomy, University of Waterloo, Waterloo, ON, N2L 3G1, Canada.*
[18]*Perimeter Institute for Theoretical Physics, 31 Caroline Street N, Waterloo, ON, N2L 1Y5, Canada.*
[19]*Department of Physics and Astronomy, University College London, Gower Street, London WC1E 6BT, UK.*
[20]*California Institute of Technology, 1200 E California Boulevard, Pasadena CA 91125, USA.*
[21]*Kavli Institute for Particle Astrophysics and Cosmology, Stanford University, 382 Via Pueblo Mall, Stanford, CA 94305-4060, USA.*

6 February 2022

ABSTRACT

Dark energy may be the first sign of new fundamental physics in the Universe, taking either a physical form or revealing a correction to Einsteinian gravity. Weak gravitational lensing and galaxy peculiar velocities provide complementary probes of General Relativity, and in combination allow us to test modified theories of gravity in a unique way. We perform such an analysis by combining measurements of cosmic shear tomography from the Canada-France Hawaii Telescope Lensing Survey (CFHTLenS) with the growth of structure from the WiggleZ Dark Energy Survey and the Six-degree-Field Galaxy Survey (6dFGS), producing the strongest existing joint constraints on the metric potentials that describe general theories of gravity. For scale-independent modifications to the metric potentials which evolve linearly with the effective dark energy density, we find present-day cosmological deviations in the Newtonian potential and curvature potential from the prediction of General Relativity to be $\Delta\Psi/\Psi = 0.05 \pm 0.25$ and $\Delta\Phi/\Phi = -0.05 \pm 0.3$ respectively (68 per cent CL).

Key words: cosmology: observations - gravitational lensing

⋆ frgs@roe.ac.uk

1 INTRODUCTION

Einstein's original formulation of General Relativity (GR) provides a remarkably precise prescription for the motions of particles in our solar system (Einstein 1916). It has survived close to a century of experimental scrutiny, beginning with the precession of Mercury's orbit and the gravitational deflection of starlight, progressing to ground-based tests with atomic clocks. Recent spaceborne tests now confirm certain predictions of GR to better than one part in ten thousand (Bertotti et al. 2003). However when we consider the behaviour of gravity on cosmological scales, which are over fourteen orders of magnitude greater than the inter-planetary distances, there is much greater scope for uncertainty. Observational evidence of an accelerating universe has called Einstein's laws into question. The underlying cause for this "dark energy" phenomenon may lie within our current understanding of gravitational physics, the leading candidate being the cosmological constant. Another possibility is that a new regime of gravitational physics has been exposed. It is this prospect which has led to a recent flurry of activity in constraining the cosmological nature of gravity (Daniel et al. 2010; Bean & Tangmatitham 2010; Zhao et al. 2010; Song et al. 2011; Reyes et al. 2010; Tereno et al. 2011; Zuntz et al. 2012; Zhao et al. 2012; Hudson & Turnbull 2012; Rapetti et al. 2012; Samushia et al. 2012).

Much like in the solar system, we are able to study the cosmological trajectories of both relativistic and non-relativistic particles, at least in a statistical sense. The peculiar motions of galaxies falling towards overdense regions generate an illusory anisotropy in their clustering pattern (Kaiser 1987), known as redshift space distortions (RSD). This effect has been observed with heightened precision over the past decade (Peacock et al. 2001; Hawkins et al. 2003; Guzzo et al. 2008; Blake et al. 2011; Beutler et al. 2012; Reid et al. 2012) permitting inferences of the rate at which cosmological structure forms. The peculiar velocities of galaxies can also be observed directly, and the inferred measurements of the growth rate are consistent with those from RSDs (see Hudson & Turnbull 2012, and references therein).

For gravitational experiments, relativistic test particles are of particular interest since their motions are not only sensitive to the effects of time dilation, but also to the curvature of space. In the classical test of GR, the deflection of starlight was observed during a solar eclipse (Dyson et al. 1920). In our experiment, distant galaxies replace nearby stars as the source of photons, our relativistic test particle. When imaging these distant galaxies, instead of measuring their gravitational deflection angles, which are unknown, we can study their shapes which appear correlated as a result of the gravitational deflection of light (Bartelmann & Schneider 2001).

One important caveat is that we are required to convert angles and redshifts into physical distances when interpreting observations of redshift space distortions and gravitational lensing. We therefore require additional information on the geometry of the universe. Geometric measurements of dark energy such as supernovae and baryon acoustic oscillations, conventionally used to determine the equation of state for dark energy, $w(z)$, are crucial for this purpose. However their measurements alone cannot distinguish modified gravity models, which are in general capable of reproducing any given wCDM expansion history. The Cosmic Microwave Background (CMB) is also used to further break degeneracies, and pro-

vides a high redshift anchor for the amplitude of density perturbations (see e.g. Komatsu et al. 2011).

Gravitational lensing is not unique in its ability to probe both metric potentials. CMB photons gain or lose energy as the potentials evolve, a phenomenon known as the Integrated Sachs Wolfe effect (ISW), leaving a significant anisotropy on the largest angular scales. In the context of a flat ΛCDM background, the expected signal strength from GR is modest, while many alternative theories of gravity can readily generate very large ISW signals, something which is not seen in the data (Lombriser et al. 2009; Zuntz et al. 2012).

While we currently lack a specific model which can compete with GR in terms of simplicity and physical motivation, there exist broad families of models such as $f(R)$ which provide useful test cases. For a recent review of the full menagerie of models, see Clifton et al. (2012). In this work we do not aim to constrain the parameter space of a particular family of models, or explicitly perform Bayesian model selection, but instead simply address the question of whether our data appear consistent with the predictions of GR. In addition to the cosmic shear data from the Canada-France-Hawaii Telescope Lensing Survey (CFHTLenS), we make use of redshift space distortions from WiggleZ and the Six-degree-Field Galaxy Survey (6dFGS).

In §2 we outline our choice of parameterisation for departures from GR. Our datasets are summarised in §3 and §4, followed by our methods and main results in §5 and §6. A comparison with alternative parameterisation schemes is presented in §7, and we briefly review the status of theoretical models of modified gravity in §8, with concluding remarks in §9.

2 PARAMETERISING THE MODIFICATION

Given the lack of a compelling model to rival GR, we choose to parameterise deviations from GR in a phenomenological manner. In effect, we simply wish to ask: is the strength of gravity the same on cosmological scales as it is here on Earth? If not, this may modify the motions of both relativistic and non-relativistic particles, but not necessarily in the same manner. Figure 1 illustrates why we are seeking a modified gravity signal on cosmological scales; it is the regime in which the classical Newtonian attraction is overwhelmed by the repulsive force associated with dark energy.

The perturbed Friedmann-Robertson-Walker metric may be expressed in terms of the scale factor $a(t)$, the Newtonian potential Ψ, and the curvature potential Φ

$$ds^2 = (1 + 2\Psi) dt^2 - a^2(t) (1 - 2\Phi) d\boldsymbol{x}^2 \,. \qquad (1)$$

In GR each of the two gravitational potentials Ψ and Φ, which carry implicit spatial and temporal dependencies, may be determined from the distribution of matter in the Universe. In Fourier space this is given by

$$k^2 \Phi_{GR} = -4\pi G a^2 \bar{\rho} \delta \,, \qquad (2)$$

where we have introduced the wavenumber k, the mean cosmic density $\bar{\rho}$, and the fractional density perturbation $\delta \equiv \rho/\bar{\rho} - 1$. In the absence of anisotropic stress the two potentials are identical, $\Psi(x,t) = \Phi(x,t)$. Relativistic particles collect equal contributions from the two potentials, since they traverse equal quantities of space and time, such that

$$k^2 \left(\Psi_{\mathrm{GR}} + \Phi_{\mathrm{GR}} \right) = -8\pi G a^2 \bar{\rho} \delta \,. \qquad (3)$$

We wish to investigate deviations from GR with a general parameterisation. Hereafter, each of the two probes, the Newtonian potential Ψ experienced by non-relativistic particles and the lensing potential $(\Phi + \Psi)$ experienced by relativistic particles, are now modulated by the parameters Σ and μ

$$\Psi(k, a) = [1 + \mu(k, a)] \, \Psi_{\mathrm{GR}}(k, a) \,, \qquad (4)$$

$$[\Psi(k, a) + \Phi(k, a)] = [1 + \Sigma(k, a)] \, [\Psi_{\mathrm{GR}}(k, a) + \Phi_{\mathrm{GR}}(k, a)] \,, \qquad (5)$$

where we have adopted notation similar to that of Amendola et al. (2008), as used more recently by Zhao et al. (2010) and Song et al. (2011). This parameterisation has the advantage of separating the modified behaviour of non-relativistic particles, as dictated by $\mu(k, a)$, from modifications to the deflection of light, as given by $\Sigma(k, a)$. By being able to reproduce a wide range of observational outcomes, in terms of the two-point weak lensing correlation functions and the growth of large scale structure, we ensure a broad sensitivity to different types of deviations from GR. There is some flexibility in how we choose to parameterise the scale and time dependence of these two parameters, much like the dark energy equation of state $w(z)$. Previous works have often chosen a scale independent model with a parameterised time variation of these functions such that $\Sigma(a) = \Sigma_s a^s$ and $\mu(a) = \mu_s a^s$. However given that our primary motivation for modified gravity is to seek an explanation of the dark energy phenomenon, we model the time-evolution to scale in proportion with the effective dark energy density implied by the background dynamics, such that

$$\Sigma(a) = \Sigma_0 \frac{\Omega_\Lambda(a)}{\Omega_\Lambda} \,, \quad \mu(a) = \mu_0 \frac{\Omega_\Lambda(a)}{\Omega_\Lambda} \,, \qquad (6)$$

where we have defined $\Omega_\Lambda \equiv \Omega_\Lambda(a = 1)$; this normalisation was chosen such that μ_0 and Σ_0 reflect the present day values of $\mu(a)$ and $\Sigma(a)$ respectively. Note that for the case of GR, $\Sigma_0 = \mu_0 = 0$. One advantage of this parameterisation is that it permits a trivial mapping between μ_0 and the popular growth index γ (Wang & Steinhardt 1998; Linder 2005). It also reduces the total number of degrees of freedom, thereby allowing us to maintain a manageable error budget. The disadvantage is that we become less sensitive to deviations from GR whose time evolution differs significantly from the adopted model. The lack of scale dependence in this model may seem questionable given the stringent Solar System tests which must be satisfied. However the length scales probed by our cosmological datasets are over fourteen orders of magnitude greater, leaving ample opportunity for a transition at scales smaller than those studied here. Furthermore, any significant departure from scale-independent growth is more readily apparent from studies of the shape of the galaxy power spectrum.

With our modified potentials in equations (4, 5) the growth of linear density perturbations is now given by

$$\delta''(a) + \left(\frac{2}{a} + \frac{\ddot{a}}{\dot{a}^2} \right) \delta'(a) - \frac{3\Omega_m}{2a^2} \left[1 + \mu(a) \right] \delta(a) = 0 \,, \quad (7)$$

while the cosmic shear power spectrum $P_\kappa^{i,j}(\ell)$ correlating redshift bins i and j takes the form
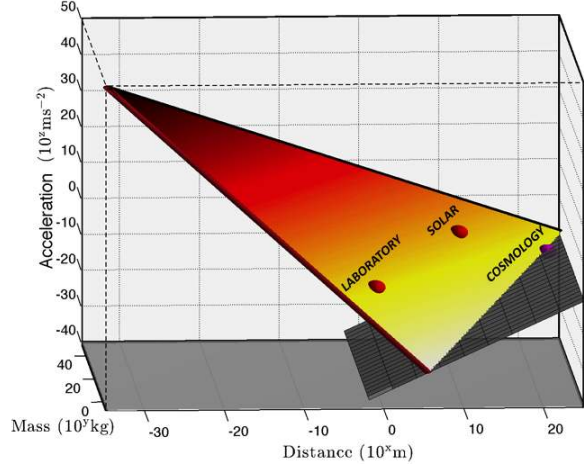
Figure 1. The shaded triangle represents the vast regime over which the gravitational acceleration of a test particle in the proximity of a mass M is thought to be well described by the Newtonian prescription $a = GMr^{-2}$. While torsion balance (Laboratory) and space-based (Solar System) tests of gravity offer superior accuracy, cosmological methods push the boundaries of our understanding of gravity. For clarity we truncate the mass axis at the Planck mass (red edge), while the upper bound (black edge) denotes the Schwarzschild radius. The grey slope illustrates the amplitude of the negative contribution arising from dark energy, which scales in proportion to r, and surpasses the conventional Newtonian force at cosmological scales.

$$P_\kappa^{i,j}(\ell) = \frac{9}{4} \Omega_m^2 \left(\frac{H_0}{c} \right)^4 \int_0^\infty \frac{g_i(\chi) g_j(\chi)}{a^2(\chi)} P_\delta \left(\frac{\ell}{f_K(\chi)}, \chi \right)$$
$$\times \left[1 + \Sigma(\chi) \right]^2 \mathrm{d}\chi \,, \qquad (8)$$

where the terms not present in the equations' conventional form are highlighted in bold. Here χ denotes the radial coordinate distance, while f_K is the comoving angular diameter distance. Note also that $P_\kappa(\ell)$ possesses an implicit dependence on μ via the time-evolution of the P_δ term. The lensing efficiency g_i is determined by the radial distribution of source galaxies $n_i(\chi)$ and the comoving angular diameter distance $f_K(\chi)$

$$g_i(\chi) = \int_\chi^\infty \mathrm{d}\chi' n_i(\chi') \frac{f_K(\chi' - \chi)}{f_K(\chi')} \,. \qquad (9)$$

Note that our parameters μ_0 and Σ_0 are only modulating the gravitational potentials in equation (1), but not the evolution of the expansion $a(t)$. The standard cosmological model, in the form of a flat ΛCDM universe, is known to provide a good description of the cosmic geometry, therefore for most of this paper we work on the assumption of this global expansion, and focus on exploring the less well determined behaviour of the gravitational perturbations. We shall also explore the consequences of adding further degrees of freedom to the expansion history, in the form of an effective dark energy equation of state w and the global curvature Ω_{K}.

3 GEOMETRIC DATA

When considering the prospect of modified gravity, we must relax the assumption that light deflection and structure formation follow the predictions of GR. This significantly exacerbates the task

of constraining all of our unknown cosmological parameters. For example, without knowing how mass bends light on cosmological scales, we cannot hope to use gravitational lensing to measure the geometry of the Universe. We therefore require auxiliary data to assist in measuring the conventional cosmological parameters, those which govern the cosmic expansion history and shape of the matter power spectrum, before we can attempt to tackle the gravitational parameters μ_0 and Σ_0.

3.1 Hubble Parameter

The current rate of cosmological expansion has long been a source of great uncertainty, largely due to the inherent difficulty in performing distance measurements. Considerable improvements have been made in the past decade, and we make use of a recent result obtained from combining observations of local supernovae, Cepheid variables, and the megamaser at the centre of NGC 4258 (Riess et al. 2011). Where stated, we include a Gaussian prior $H_0 = 73.8 \pm 2.4 \, \mathrm{km\,s^{-1}\,Mpc^{-1}}$ from Riess et al. (2011). In de Sitter space this would correspond to the distance between any two comoving points doubling every thirteen billion years.

Since it is common practice to assume GR in most astronomical and cosmological studies, extra care must be taken when adopting quoted results from previous studies. For example, the determination of the distance to water masers is based on the assumption of Keplerian motions. Furthermore the pulsation of Cepheids relies on the star's self-gravitation, therefore unusual gravitational behaviour could lead to a modification of their period-luminosity relation. However there are currently no signs of anomalous behaviour in the data (Jain et al. 2012).

3.2 Baryon Acoustic Oscillations

Encoded within the distribution of galaxies is a useful comoving ruler, a modest excess of galaxy pairs at $\sim$150 Mpc, relating to the distance sound waves were able to propagate prior to recombination. In Fourier space this feature is referred to as the Baryon Acoustic Oscillations (hereafter BAO). For a given BAO observation, the relevant cosmological information can often be distilled to a single datapoint, that of $D_{\mathrm{V}}(z)/r_{\mathrm{s}}$, where r_s is the sound horizon at the baryon drag epoch, and the volume element $D_{\mathrm{V}}(z)$ is defined in terms of the angular diameter distance $D_{\mathrm{A}}(z)$ and Hubble parameter $H(z)$

$$D_{\mathrm{V}}(z) \equiv \left[(1+z)^2 D_{\mathrm{A}}^2(z) \frac{cz}{H(z)} \right]^{\frac{1}{3}} . \qquad (10)$$

The most conservative treatment of BAO data would be to treat r_s as an unknown quantity, and eliminate it by taking the ratio of $D_{\mathrm{V}}(z)$ at two separate redshifts. However since the CMB provides us with a good understanding of the conditions in the early Universe, we have the opportunity to determine r_s for a given set of cosmological parameters. For our purposes this quantity is derived using equation (6) from Eisenstein & Hu (1998).

Where stated, we utilise measurements of $D_{\mathrm{V}}(z)/r_{\mathrm{s}}$ at two different redshifts. Anderson et al. (2012) present BAO constraints from the Baryon Oscillation Spectroscopic Survey (BOSS), and we also include a measurement from the Sloan Digital Sky Survey (SDSS) Luminous Red Galaxies (Padmanabhan et al. 2012). Both studies present results before and after a reconstruction method has been applied, a technique which increases the prominence of the

BAO by partially reversing the effects of gravitational infall. We conservatively adopt the BAO results prior to reconstruction, since we wish to avoid making assumptions relating to the growth of density perturbations. The change in our results is negligible, however, when the reconstructed values are included. For the BOSS CMASS sample, the 'consensus' result (Anderson et al. 2012) averages the power spectrum and correlation function analyses, giving $D_{\mathrm{V}}/r_{\mathrm{s}}(z = 0.57) = 13.67 \pm 0.22$. The SDSS datapoint is given by $D_{\mathrm{V}}/r_s(z = 0.35) = 8.89 \pm 0.31$. We neglect any covariance in the two data points generated by the small overlap between the SDSS and BOSS volumes, which spans less than 9% of the BOSS volume (Anderson et al. 2012).

It should be noted that when combined with WMAP7, recent BAO results suggest values of H_0 which are in mild tension with the measurement from Riess et al. (2011). For example Anderson et al. (2012) find $H_0 = 68.4 \pm 1.3 \, \mathrm{km\,s^{-1}\,Mpc^{-1}}$, while studies from 6dFGS and SDSS measure $67 \pm 3.2 \, \mathrm{km\,s^{-1}\,Mpc^{-1}}$ and $69.8 \pm 1.2 \, \mathrm{km\,s^{-1}\,Mpc^{-1}}$ respectively (Beutler et al. 2011; Mehta et al. 2012). We present separate results generated using the H_0 and BAO data in Section 6.

3.3 Cosmic Microwave Background ($\ell > 100$)

We utilise the temperature C_ℓ^{TT} and polarisation C_ℓ^{TE} spectra from the WMAP 7-year data (Larson et al. 2011). This serves two purposes, first it offers strong constraints on a number of cosmological parameters, but it also serves to directly assist in the measurement of the growth of structure. Our current position in space and time, $z = 0$, acts as the benchmark from which all cosmological distance measurements are made. However when mapping the growth of structure, it is the epoch of recombination at $z \simeq 1100$ which effectively acts as our starting point. The CMB provides a precise measure of the amplitude of density fluctuations in the early Universe. Combining this with a measure of the clustering amplitude at low redshift provides a strong lever for constraining the growth rate between these two epochs.

Large angular scales of the CMB are sensitive to modified gravity models, and these are treated separately in §4.3. The implications for modified gravity have already been studied (see for example Zuntz et al. 2012), and here our primary focus is to explore the constraints available from lensing. For the range of values considered in this study, μ_0 and Σ_0 were found to impose negligible change in either C_ℓ^{TT} or C_ℓ^{TE} beyond the $\ell = 100$ multipole (see Section 4.3). Unless otherwise stated we simply truncate the largest angular scales, such that only $\ell \geqslant 100$ are included in our analysis. In doing so we negate the impact of the ISW, and utilise WMAP7 only to assist in measuring the conventional cosmological parameters. For further details of our treatment of the CMB, see Appendix A.

4 GRAVITATIONAL DATA

4.1 Cosmic Shear

Gravitational lensing by large scale structures in the Universe coherently distort the observed shapes of distant galaxies. This cosmic shear distortion can be used to directly probe dark matter, and, when analysed in tomographic redshift bins, can also reveal the growth of structure. It also acts as a useful tool for testing the laws of gravity (White & Kochanek 2001; Doré et al. 2007). We use tomographic cosmic shear data from CFHTLenS, published in Ben-
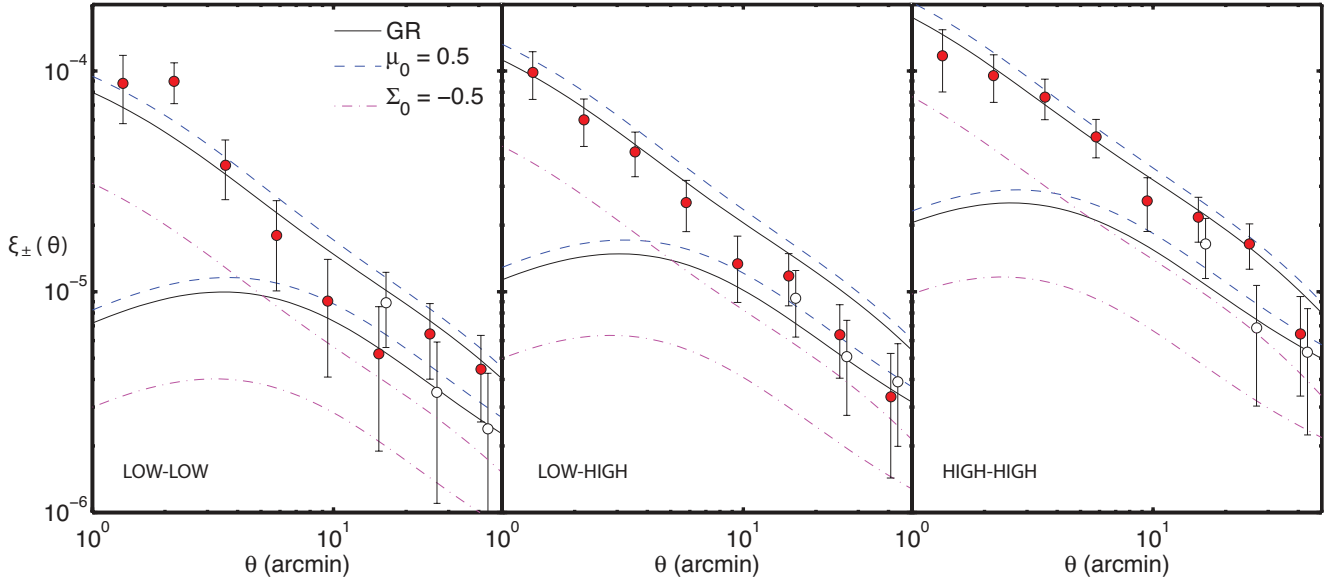
Figure 2. The cosmic shear data from CFHTLenS. Each panel contains the two lensing correlation functions, $\xi_+(\theta)$ (filled) and $\xi_-(\theta)$ (empty) with the $\xi_-(\theta)$ points slightly offset for clarity. The source galaxies are divided into two redshift bins, a 'low' redshift bin with $0.5 < z \leqslant 0.85$ and a 'high' redshift bin with $0.85 < z \leqslant 1.3$. The left, middle and right hand panels display data from the low-low, low-high, and high-high correlations. In each case, the black lines are the set of theoretical curves corresponding to $\xi_+(\theta)$ (upper) and $\xi_-(\theta)$ (lower) for the best-fitting ΛCDM cosmology. The dashed lines correspond to a cosmological model with the same expansion history $H(z)$ as the best-fitting model, but with a boost in the effective gravitational constant ($\mu_0 = 0.5$; $\Sigma_0 = 0$). The dot-dashed lines demonstrate the signal one expects if the present-day ($z = 0$) gravitational potentials are associated with Newtonian gravity ($\mu_0 = 0$; $\Sigma_0 = -0.5$).

jamin et al. (2012). CFHTLenS is a 154 square degree deep multi-colour survey optimised for weak lensing analyses, where the data were obtained as part of the CFHT Legacy Survey on the 3.6m CFHT. Weak gravitational lensing is widely recognised as one of the most powerful probes of cosmology, but also one of the most technically challenging, as the weak cosmic shear distortion must be separated from other sources of image distortion induced by the atmosphere, telescope and detector. The CFHTLenS analysis represents the current state-of-the-art in weak lensing data processing (Erben et al. 2009), weak lensing measurement (Miller et al. 2012), photometric redshift measurement (Hildebrandt et al. 2012), and systematic error analysis (Heymans et al. 2012). Benjamin et al. (2012) also use an angular cross-correlation analysis to verify the accuracy of the measured redshift distributions that we use in this analysis. These results, in combination with the cosmology insensitive joint shear-redshift systematic test presented in Heymans et al. (2012), allows us to conclude that the analysis of the survey data is robust within our uncertainties and residual systematics levels and can therefore be used to test the laws of gravity.

Benjamin et al. (2012) analyse two high-redshift bins with $0.5 < z \leqslant 0.85$ and $0.85 < z \leqslant 1.3$, presenting the auto-correlation and cross-correlations of the angular two-point shear correlation functions $\xi_\pm^{ij}(\theta)$ over scales $1 < \theta < 40$ arcmin, as shown in Figure 2. The choice to use only two broad high red-shift bins in this tomographic analysis was motivated by the desire to mitigate the impact of intrinsic galaxy alignments on the tomographic measurements (see for example Heymans et al. 2006; Joachimi et al. 2011, and references therein). For this combination of high redshift bins, the contamination to the signal is expected to be at the percent level and so we follow Benjamin et al. (2012) by neglecting this source of error in our analysis. We use a covariance matrix between the resulting correlated data points as estimated

from N-body lensing simulations (Harnois-Déraps et al. 2012), discussed and verified in Kilbinger et al. (2012) and Benjamin et al. (2012).

Theoretical predictions for these correlation functions are generated using the relation

$$\xi_\pm^{i,j}(\theta) = \frac{1}{2\pi} \int_0^\infty P_\kappa^{i,j}(\ell)\, \mathrm{J}_{0/4}(\ell\theta)\, \ell\, \mathrm{d}\ell \,, \tag{11}$$

where $P_\kappa^{i,j}(\ell)$ is given in equation (8) and $\mathrm{J}_{0/4}$ are the zeroth and fourth order Bessel functions.

On the smallest angular scales studied by cosmic shear it is likely that baryonic physics will disturb the density perturbations (Semboloni et al. 2011). This is also the regime where our prescription for modelling the non-linear correction to the matter power spectrum (see below) begins to break down. Due to the very different nature of the zeroth and fourth Bessel functions, the $\xi_-(\theta)$ correlation function is sensitive to considerably smaller scales than $\xi_+(\theta)$ for a given θ value. For the ξ_- statistic we therefore only include the larger angular scales $\theta > 10'$. These data points are presented in Figure 2, alongside theoretical predictions from the best-fit ΛCDM cosmology and two illustrative modified gravity scenarios. From left to right, the three panels in Figure 2 relate to the correlations of the low-low, low-high, and high-high redshift bins. A more detailed justification for the angular cuts and their implications are discussed in Benjamin et al. (2012); in any case we find no significant change in our results when the small angular scales of $\xi_-(\theta)$ are included due to the high correlation between the points and their relatively low signal-to-noise. We further investigate the impact of truncating smaller length scales in Kitching et al (in prep).

4.2 Redshift Space Distortions

Doppler distortions of the galaxy clustering pattern provide an independent probe of gravitational physics, by revealing the coherent flows of galaxies which trace the growth of cosmic structure. The principal effect on large scales is an amplification of apparent galaxy clustering along the line-of-sight, breaking the statistical isotropy. This anisotropy can be extracted from the 2-point clustering statistics of a galaxy redshift survey, yielding a measurement of $f(z)\sigma_8(z)$. Here f is the growth rate of structure, expressible in terms of the growth factor $D(a)$ as $f \equiv d\ln D/d\ln a$ where the growth factor describes the evolution of the amplitude of a single linear density perturbation $\delta(a) = D(a)\delta(1)$. The function $\sigma_8(z)$ quantifies the amplitude of the linear clustering of matter at a given redshift, and is defined as the r.m.s. density variation in spheres of comoving radius $8\ h^{-1}\mathrm{Mpc}$. The degeneracy between f and σ_8 arises due to the unknown galaxy bias factor b: the observables are the anisotropy in the galaxy clustering pattern which depends on $\beta \equiv f/b$, and the galaxy clustering amplitude which depends on $b\sigma_8(z)$.

Measurements of redshift-space distortions from a galaxy redshift survey are degenerate with a second isotropy-breaking mechanism: the Alcock-Paczynski distortion (Alcock & Paczynski 1979), which arises if the fiducial cosmological model we adopt for converting redshifts and angles to physical distances differs from the true cosmological model (Ballinger et al. 1996; Matsubara & Suto 1996; Seo & Eisenstein 2003; Simpson & Peacock 2010). The amplitude of Alcock-Paczynski anisotropy depends on the quantity

$$F(z) = (1+z)D_\mathrm{A}(z)H(z)/c, \qquad (12)$$

in terms of the angular diameter distance $D_A(z)$ and Hubble expansion parameter $H(z)$. Although measurements of F and $f\sigma_8$ from a galaxy redshift survey are strongly correlated, the angular distortions imprinted in the clustering pattern by these two effects are sufficiently different that the degeneracy can be broken.

The measurements of $(f\sigma_8, F)$ that we use in this study are derived from the WiggleZ Dark Energy Survey published in Blake et al. (2012) and from 6dF Galaxy Survey (6dFGS), as presented in Beutler et al. (2012). Figure 3 compares the measurements of $f\sigma_8$ from WiggleZ (squares) and the 6dFGS (diamond) to the best-fit ΛCDM cosmology and two example modified gravity scenarios with $\mu_0 = 0.5$ and $\mu_0 = 1.0$ (dashed).

The WiggleZ Survey (Drinkwater et al. 2010) at the 3.9-m Anglo-Australian Telescope has mapped a cosmic volume ~ 1 Gpc^3 over the redshift range $0 < z < 1$. By covering a total of ~ 800 deg^2 of sky the WiggleZ survey mapped about 100 times more effective cosmic volume in the $z > 0.5$ Universe than previous galaxy redshift surveys. Target galaxies were chosen by a joint selection in UV and optical wavebands, using observations by the Galaxy Evolution Explorer satellite (GALEX) (Martin et al. 2005) matched with ground-based optical imaging from the Sloan Digital Sky Survey (York et al. 2000) in the Northern Galactic Cap, and from the Red Sequence Cluster Survey 2 (RCS2) (Gilbank et al. 2011) in the Southern Galactic Cap. A series of magnitude and colour cuts (Drinkwater et al. 2010) were used to preferentially select high-redshift star-forming galaxies with bright emission lines, that were then observed using the AAOmega multiobject spectrograph (Sharp et al. 2006) in 1-hr exposures.

The 6dFGS is a near-infrared selected combined redshift and peculiar velocity survey covering nearly the entire southern sky with Galactic latitude $|b| < 10°$. It was undertaken with the Six-
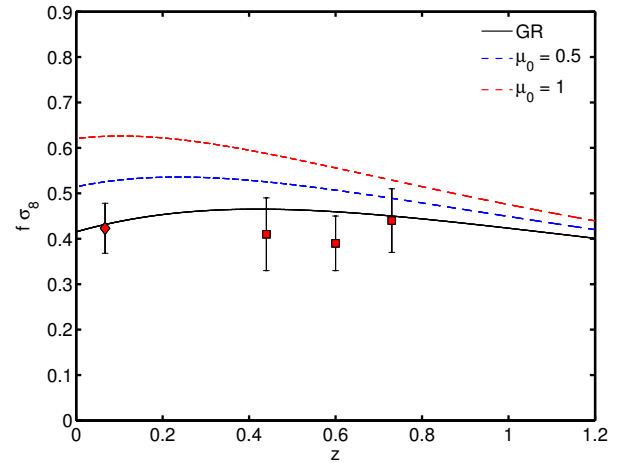

Figure 3. The growth data from WiggleZ (Blake et al. 2012) and 6dFGS (Beutler et al. 2012). The black line is the corresponding theoretical curve for the best-fit ΛCDM cosmology. The dashed lines correspond to the same cosmology but with a boost in effective gravitational constant μ_0.

Degree Field (6dF) multi-fibre instrument on the UK Schmidt Telescope from 2001 to 2006 (Jones et al. 2004, 2009). The redshift survey covers 125,000 galaxies with $8.75 \leqslant K \leqslant 12.75$ and median redshift $z = 0.052$.

In this study we use the WiggleZ joint measurements of $(f\sigma_8, F)$ in three different redshift slices with effective redshifts $z = 0.44$, 0.60, and 0.73. The marginalised measurements of the growth rate in these redshift slices are $f\sigma_8(z) = (0.41 \pm 0.08, 0.39 \pm 0.06, 0.44 \pm 0.07)$. The marginalised measurements of the Alcock-Paczynski distortion parameter are $F = (0.48 \pm 0.05, 0.65 \pm 0.05, 0.86 \pm 0.07)$. The correlation coefficients between these pairs of values are $(0.73, 0.74, 0.85)$. These measurements were derived by fitting the non-linear clustering model provided by Jennings et al. (2011) to the 2D WiggleZ power spectrum over the range of wavenumbers $0 < k < 0.2\,h\,\mathrm{Mpc}^{-1}$, marginalising over the linear galaxy bias factor and a small-scale velocity dispersion σ_v. Blake et al. (2011) carried out a suite of systematics tests to demonstrate that the derived results did not depend on either the fitting range or the non-linear model of redshift-space distortions adopted; we refer the reader to this paper for further details. There is some overlap (~ 500 sq. degrees) between the sky areas surveyed by WiggleZ and the SDSS/BOSS surveys that are used in our results which are stated to include BAO. However, based on the nature of the geometric BAO data being very different to that used for the RSD gravitational measurements we assume that any covariance in these derived results is negligible. In essence, when considering the redshift-space galaxy power spectrum, the location of the acoustic peak bears little connection to the power of the quadrupole.

We also include the single datapoint $f\sigma_8(z = 0.067) = 0.423 \pm 0.055$ (Beutler et al. 2012) from the 6dFGS. Due to its low redshift, this result benefits from having negligible sensitivity to the Alcock-Paczynski distortion, and a large sensitivity to our modified gravity parameter μ_0, as can be seen in Figure 3. The 6dFGS measurement was derived using the non-linear model of Jennings et al. (2011), including wide-angle corrections, fit to the 2D galaxy redshift-space correlation function for transverse separations $r_p > 16\,h^{-1}$ Mpc. The growth-rate measurements obtained, marginalized over bias, were consistent with fitting an empirical streaming model to the results (see Beutler et al. 2012, for further
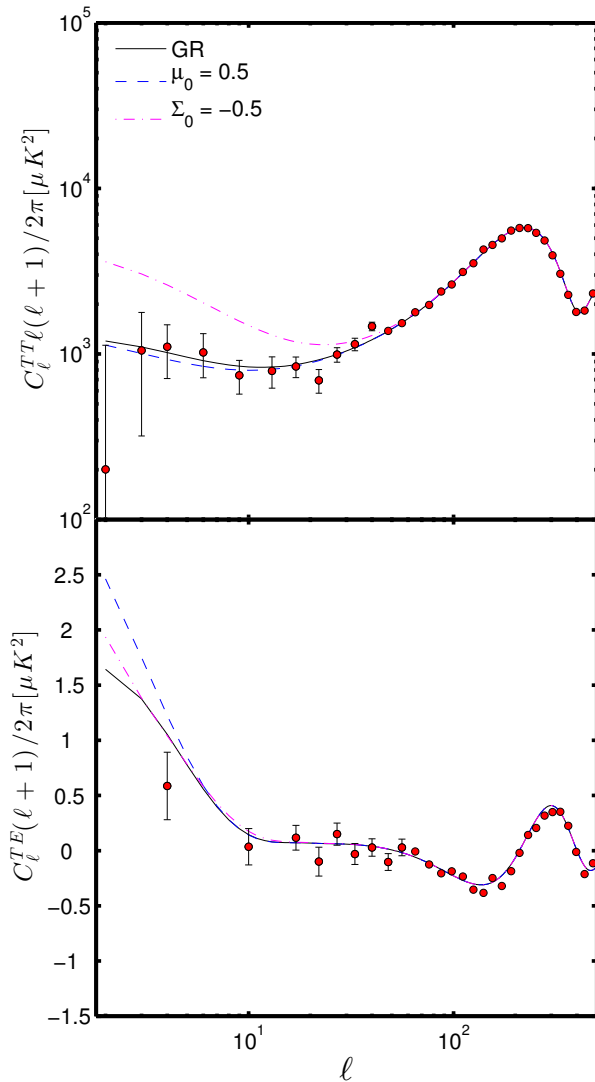
Figure 4. Modifications to the temperature (upper panel) and temperature-polarisation (lower panel) power spectra of the CMB. In each panel the black line is the corresponding theory curves for the best-fitting ΛCDM cosmology. The dashed and dash-dot lines represent the same modifications to our modified gravity parameters as seen in Figure 2. Superposed on these theoretical predictions are the binned data points from the 7−year WMAP observations (Larson et al. 2011).

details). While the WiggleZ and 6dFGS analyses differ in their utilisation of the power spectrum and correlation function respectively, their approach to modelling non-linear corrections and galaxy bias remains consistent.

4.3   Cosmic Microwave Background ($\ell < 100$)

When in the presence of a time-dependent gravitational potential, a particle may extract or lose energy from its surroundings. It is this mechanism which space probes exploit when passing close to planets for a gravitational slingshot. For CMB photons, the gravitational source is associated with large scale density perturbations. In GR, if the photon passes through a high density region of the Universe, the dark energy-induced decay of the gravitational potentials $\Phi(x,t)$ and $\Psi(x,t)$ results in a net energy gain, with a blue-shifting effect. Conversely, passing through a void results in a net loss of en-

ergy. The resulting temperature perturbation may be expressed by the line integral

$$\frac{\Delta T}{T} = -\int \frac{\mathrm{d}}{\mathrm{d}\eta} \left[\Phi(x,t) + \Psi(x,t) \right] \mathrm{d}\eta, \qquad (13)$$

where η is the conformal time defined by $\mathrm{d}\eta \equiv \mathrm{d}t/a$, and the integral follows the path of the photon. We can see from equation (13) that this ISW effect is another probe which, like gravitational lensing, retains sensitivity to both gravitational potentials. However the ISW signal within the temperature anisotropies is only expected to be significant on large angular scales, $\ell < 100$ as illustrated by Figure 4 which compares the temperature (upper) and temperature-polarisation (lower panel) GR power spectra of the CMB (solid) with data points used in this analysis, from the 7−year WMAP observations (Larson et al. 2011). The dashed and dash-dot lines represent the same modifications to our modified gravity parameters as seen in Figure 2 with $\mu_0 = 0.5; \Sigma_0 = 0$ (dashed) and $\mu_0 = 0; \Sigma_0 = -0.5$ (dot-dashed). These modified gravity models of the CMB power spectrum deviate from GR only on the largest angular scales. Observational ISW studies are therefore heavily restricted by cosmic variance, and future experiments cannot be expected to improve upon WMAP, unless we begin to include cross-correlations with large-scale structure. Note that throughout this work, we use the term ISW to refer to the phenomenon which arises in the CMB power spectrum, not the cross-correlation between the CMB and the distribution of galaxies.

For any metric theory of gravity, density fluctuations on scales beyond the horizon are subject to a stringent consistency relation. Since material cannot be transported at superluminal velocities, superhorizon perturbations are destined to evolve along a path determined by the global expansion (Bertschinger 2006). Therefore the constraints presented which incorporate the ISW should be treated with this in mind, as the ISW involves scales very much larger than those studied by gravitational lensing, a regime where there is a stronger expectation that the values of μ_0 and Σ_0 are close to zero.

5   METHODS

Using a combination of geometric data (presented in §3) and gravitational data (presented in §4), we use a maximum likelihood analysis to constrain our phenomenological modified gravity parameters μ_0 and Σ_0.

To generate the likelihood values we modified CosmoPMC (Kilbinger et al. 2011), an adaptive importance sampling code, to incorporate the alterations to the growth of structure (equation 7) and cosmic shear signal (equation 8). A customised version of MGCAMB (Hojjati et al. 2011; Lewis et al. 2000) was used to evaluate the CMB anisotropies for a given set of cosmological parameters, which are then assessed with the WMAP likelihood code[1]. Our analysis spans the parameter set $\{\Omega_m, \Omega_b, h, \tau, n_s, A_{SZ}, \Delta_{\mathrm{R}}^2, \mu_0, \Sigma_0\}$, where τ is the optical depth, n_s the spectral index, A_{SZ} the amplitude of the Sunyaev-Zel'dovich template for the CMB (Komatsu & Seljak 2002; Spergel et al. 2007), and Δ_{R}^2 controls the primordial amplitude of matter perturbations. Where specified we also marginalise over a time-independent effective equation of state for dark energy w and global curvature Ω_{K}, in addition to the aforementioned set of parameters. We adopt flat priors throughout, spanning the following

[1] http://lambda.gsfc.nasa.gov

parameter ranges: $\Omega_m \in [0.05; 1]$, $\Omega_b \in [0.01; 0.1]$, $h \in [0.5; 1]$, $\tau \in [0.02; 0.3]$, $n_s \in [0.8; 1.2]$, $A_{SZ} \in [0; 2]$, $\Delta_R^2 \in [1.8; 3.5] \times 10^{-9}$, $\mu_0 \in [-4.0; 4.0]$, $\Sigma_0 \in [-4.0; 4.0]$, $w \in [-1.5; -0.3]$, and $\Omega_K \in [-0.1; 0.1]$. In most cases these boundaries extend well beyond the regions of high likelihood, except for A_{SZ} which is not well constrained, however its impact on the other parameters is negligible. In order to generate visualisations of the generated samples we make use of code adapted from CosmoloGUI[2].

In generating the matter power spectrum, the CosmoPMC package makes use of the Eisenstein & Hu (1998) transfer function. The growth factor is determined in accordance with the modified equation (7), before adding a nonlinear correction using the prescription of Smith et al. (2003). To compensate for cosmologies where $w \neq -1$, a further modulation of the nonlinear power is required, as presented in McDonald et al. (2006). We make use of the scaling correction provided in Schrabback et al. (2010) to apply this formalism across our full range of parameter space. However it should be noted that our results only have a weak dependence on this correction. The mean values of μ_0, Σ_0, and w all change by less than 0.02 when the prescription from Schrabback et al. (2010) is omitted, which is well within our statistical errors. The value of the Σ_0 parameter has no impact on structure formation, and while we may expect nonzero values of μ_0 to alter the nonlinear correction to the matter power spectrum, we do not attempt to correct for it here. We expect the prescription of Smith et al. (2003) to remain a reasonably good approximation in the presence of a simple scale-independent modification to the growth of structure such as that induced by μ_0. To first order the correction associated with nonlinear power is simply a function of the ambient linear power at that epoch; how quickly it arrives at this state is of less importance. In any case, modified behaviour on nonlinear scales would still weaken the fit to the data achievable within the framework of GR.

6 RESULTS

6.1 ΛCDM

We begin with the simple case of a flat ΛCDM geometry. In this scenario we are making a strong assumption about the form of the cosmic expansion history $H(z)$, but in doing so make significant gains in the precision of our likelihood contours. Any apparent deviation from GR witnessed at this stage must be interpreted with caution due to the strong assumptions of this relatively simple model.

The left panel of Figure 5 illustrates the variety of 1– and 2– σ confidence intervals for different combinations of datasets. Each of these contours include the auxiliary data of WMAP7 ($\ell \geqslant 100$) and a prior on H_0. The horizontal (green) contours reflect the pure μ_0 measurement established with the WiggleZ data. The Σ_0 parameter is unconstrained since the peculiar motions of galaxies are slow ($v \ll c$), and are therefore insensitive to the spatial curvature $\Phi(x, t)$. The near-vertical (red) contours correspond to the cosmic shear data from CFHTLenS. Unsurprisingly, this is predominantly a measure of Σ_0 due to its direct influence on the lensing potential. The mild sensitivity to μ_0 arises from the amplitude of the matter power spectrum entering in equation (8). A positive value of μ_0 enhances the growth of structure and thus strengthens the cosmic shear signal (for a given primordial amplitude). This can

[2] http://www.sarahbridle.net/cosmologui

be offset with a negative value of Σ_0, weakening the deflection of light and leading to the negatively-sloped degeneracy direction seen in the red contours of Figure 5. When combined (blue), the near-orthogonal degeneracy directions of WiggleZ and CFHTLenS produce a considerable reduction in the permitted area of parameter space. The tightest constraints (white) emerge from adding in BAO from BOSS and the ISW large scale anisotropies ($\ell < 100$) from WMAP7. None of these combinations show any preference for non-zero values of either μ_0 or Σ_0, suggesting that GR remains a successful model of gravitation on cosmological scales, for both relativistic and non-relativistic particles.

The mean and 1-σ errors in the modified gravity parameters are found to be $\mu_0 = 0.05 \pm 0.25$ and $\Sigma_0 = 0.00 \pm 0.14$. The results for other combinations of datasets can be found in Table 1.

How sensitive are we to the choice of auxiliary data? The right hand panel of Figure 5 contains the same datasets and layout as the left hand panel, except here we have replaced the prior on H_0 with the BAO data summarised in Section 3.2. The BAO prefer a higher value of Ω_m (or equivalently, a lower value of H_0), and this does push the lensing data to predict a lower value of σ_8, which pushes the bulk of the likelihood towards negative values for Σ_0. This results in constraints of $\mu_0 = -0.12 \pm 0.23$ and $\Sigma_0 = -0.17 \pm 0.10$. The combination of CFHTLenS and RSD data (blue) can be compared with the constraints derived from the full WMAP7 power spectra, including the ISW, and BAO (yellow).

6.2 wCDM

The dangers of confusing the signatures of modified geometry and modified gravity have previously been highlighted in the literature (see for example Simpson & Peacock 2010). In order to claim that we are testing GR and not simply ΛCDM we must therefore allow greater freedom in the cosmic expansion history $H(z)$. This is inevitably accompanied by some loss of precision, so we shall restrict ourselves to adding one extra parameter. In Figure 6 we utilise both H_0 and BAO, in combination with CFHTLenS, RSD and the small angular scales of WMAP7, conservatively omitting the ISW information for the reasons outlined in Section 4.3. While the green contour in the left panel corresponds to the standard flat ΛCDM background, the blue contours presented in the left and centre panels allow the effective dark energy equation of state w to deviate from -1. The centre panel illustrates a degeneracy which causes the confidence contours to broaden. More positive values of w lead to a greater prevalence of dark energy at higher redshift (for a given value of Ω_m) and thus a slowing of the growth of structure. This can be compensated by enhancing the value of μ, which accelerates the growth of structure, leading to a similar growth history $f(z)$ to GR. For a wCDM cosmology the mean and 68 per cent confidence intervals are given by $\mu_0 = -0.59 \pm 0.34$, $\Sigma_0 = -0.19 \pm 0.11$, and $w = -1.19 \pm 0.1$. More detailed results are presented in Table 1.

6.3 owCDM

We further generalise the expansion history by allowing for nonzero values of the global curvature Ω_k, using the same combination of data sets as in §6.2. The red contours in all three panels of Figure 6 demonstrate the relatively small impact that non-flat geometries have on our confidence limits. The mean and 68 per cent confidence intervals are given by $\mu_0 = -0.65 \pm 0.34$, $\Sigma_0 = -0.26 \pm 0.12$, $\Omega_k = 0.096 \pm 0.087$, and $w = -1.16 \pm 0.10$.
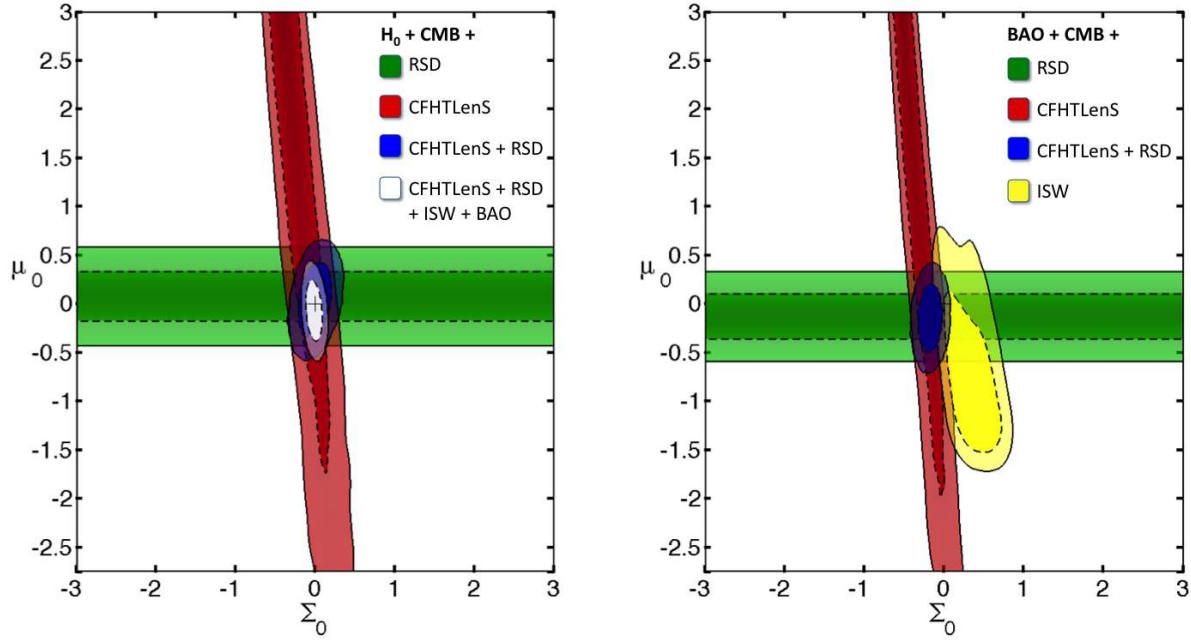
Figure 5. *Left:* Constraints on the modified gravity parameters in a flat ΛCDM background from redshift space distortions (green), weak lensing (red), and combined (blue). (68 and 95 per cent CL). The dashed and solid contours represent the 68 and 95 per cent condence intervals respectively. Two auxiliary datasets are used here to break degeneracies with the conventional cosmological parameters. These are the small-angle anisotropies from WMAP7 ($\ell \geqslant 100$), and a prior on H_0 from (Riess et al. 2011). The cross positioned at the origin denotes the prediction of General Relativity. *Right:* The red, green and blue contours are the same as the left panel, except the prior on H_0 has been replaced by measurements of the Baryon Acoustic Oscillations as detailed in Section 3.2. The yellow contours signify the constraints derived from the full WMAP7 power spectra, including the large angular scales ($\ell < 100$). The white contours in the left hand panel show the constraints when all data sets are analysed in combination.

Table 1. Parameter constraints for different combinations of dataset and parameter space. The three different backgrounds we explore are flat ΛCDM, flat wCDM and the non-flat wCDM which we denote as owCDM. All constraints make use of the small scale anisotropies from WMAP7 ($\ell \geqslant 100$), while those marked ISW also utilise the larger angular scales.

Background	Data (+ CMB + H_0)	μ_0	Σ_0	Ω_m	H_0	σ_8	w	Ω_K
ΛCDM	CFHTLenS	1.2 ± 2.2	-0.17 ± 0.28	0.260 ± 0.024	71.3 ± 2.3	0.96 ± 0.24	$\cdots$	$\cdots$
ΛCDM	RSD	0.08 ± 0.25	$\cdots$	0.254 ± 0.023	71.8 ± 2.2	0.801 ± 0.024	$\cdots$	$\cdots$
ΛCDM	CFHTLenS + RSD	0.05 ± 0.25	0.00 ± 0.14	0.256 ± 0.023	71.6 ± 2.2	0.804 ± 0.023	$\cdots$	$\cdots$
wCDM	CFHTLenS + RSD + BAO	-0.59 ± 0.34	-0.19 ± 0.11	0.272 ± 0.015	71.7 ± 1.8	0.820 ± 0.025	-1.19 ± 0.10	$\cdots$
owCDM	CFHTLenS + RSD + BAO	-0.65 ± 0.34	-0.26 ± 0.12	0.289 ± 0.021	71.6 ± 1.8	0.833 ± 0.028	-1.16 ± 0.10	0.0096 ± 0.0087
Background	Data (+ CMB + BAO)	μ_0	Σ_0	Ω_m	H_0	σ_8	w	Ω_K
ΛCDM	CFHTLenS	1.0 ± 2.2	-0.31 ± 0.24	0.305 ± 0.018	67.2 ± 1.4	0.95 ± 0.24	$\cdots$	$\cdots$
ΛCDM	RSD	-0.13 ± 0.23	$\cdots$	0.300 ± 0.017	67.5 ± 1.4	0.807 ± 0.023	$\cdots$	$\cdots$
ΛCDM	ISW	-0.62 ± 0.64	0.34 ± 0.22	0.294 ± 0.015	68.2 ± 1.2	0.768 ± 0.068	$\cdots$	$\cdots$
ΛCDM	CFHTLenS + RSD	-0.12 ± 0.23	-0.17 ± 0.10	0.300 ± 0.017	67.6 ± 1.4	0.807 ± 0.023	$\cdots$	$\cdots$
ΛCDM	CFHTLenS + RSD + ISW + H_0	-0.06 ± 0.21	-0.010 ± 0.068	0.273 ± 0.010	70.10 ± 0.97	0.803 ± 0.022	$\cdots$	$\cdots$

7 ALTERNATIVE PARAMETERISATIONS

In this section we consider the relationship between the (μ, Σ) parameterisation adopted in this work, and three other popular parameterisations.

7.1 γ Parameter

A widely adopted parameterisation for quantifying anomalous structure growth is the growth index γ (Wang & Steinhardt 1998; Linder 2005)

$$f(z) \simeq \Omega_m^\gamma(z), \qquad (14)$$
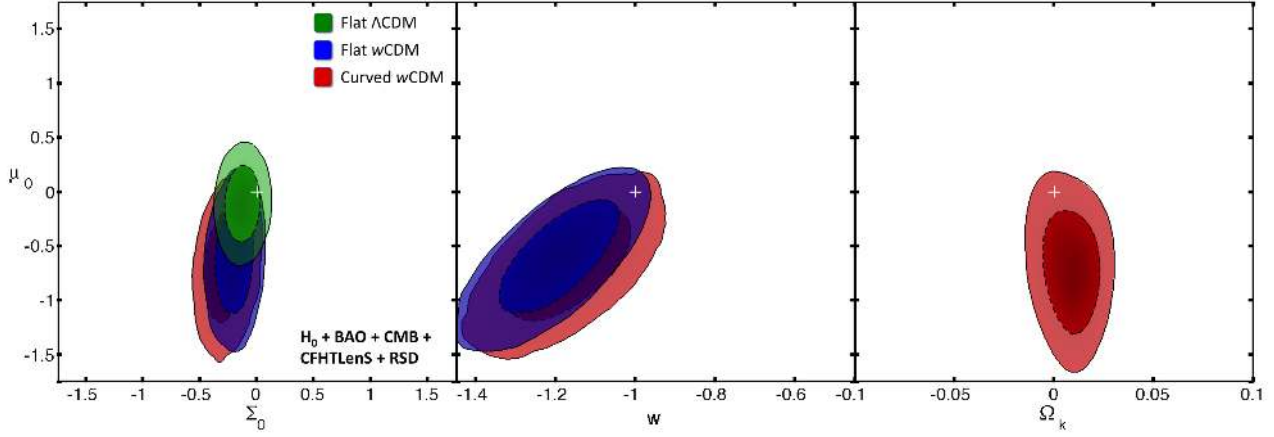
Figure 6. In this figure we extend our analysis to more general expansion histories. All of the above contours use a combination of cosmic shear and redshift space distortions, combined with the geometric constraints from H_0, BAO, and WMAP7 ($\ell \geqslant 100$). The green set of contours in the left panel corresponds to the background expansion of flat ΛCDM. For the blue contours in the left and centre panels we allow the effective dark energy equation of state to deviate from $w = -1$, highlighting a significant degeneracy in the $w - \mu_0$ plane. Finally, the red contours appearing in each of the panels allow non-zero curvature in addition to the wCDM background.
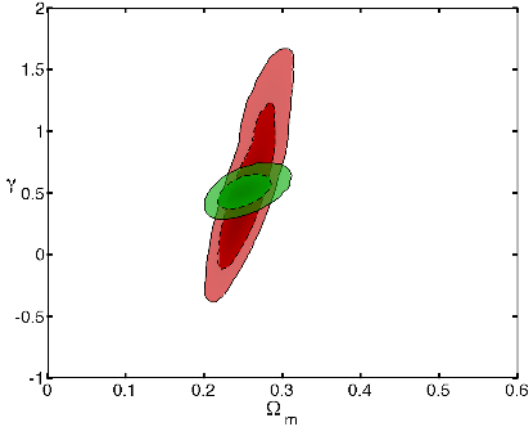
Figure 7. Confidence limits in the γ - Ω_m plane, as derived from redshift space distortions (WiggleZ + 6dFGS) in green, and cosmic shear (CFHTLenS) in red (68 and 95 per cent CL), using small-angle anisotropies from WMAP7 ($\ell \geqslant 100$), and a prior on H_0 as auxillary data sets. Note that here γ is the only modified gravity parameter, as we have set $\Sigma(a) = 0$.

where setting $\gamma = 0.55$ offers an estimate of the growth factors in wCDM cosmologies with sub-percent accuracy. Equation (23) from Linder & Cahn (2007) gives us the relation

$$\gamma = \frac{3 \left[1 - w - \frac{\mu(a)}{1 - \Omega_m(a)} \right]}{5 - 6w}, \tag{15}$$

for a constant equation of state w. In a flat ΛCDM Universe, this parameter may be expressed as a simple function of μ_0 and Ω_Λ,

$$\gamma = \frac{6}{11} \left[1 - \frac{\mu_0}{2\Omega_\Lambda} \right]. \tag{16}$$

Applying the prescription for the growth rate in equation (14) with a constant value the γ parameter does not offer a perfect re-
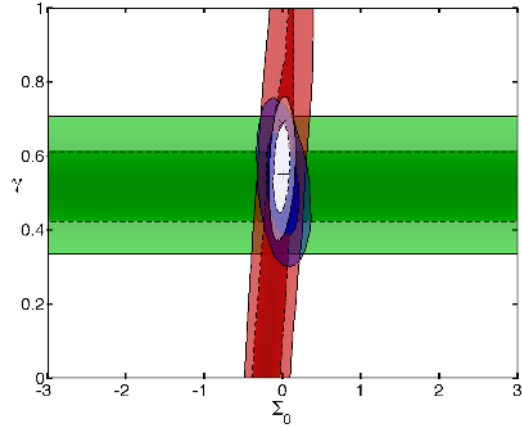
Figure 8. The same combinations of data as the left hand panel of Figure 5, except we have replaced the μ_0 parameter with γ using the relation given by equation (16).

production of the growth of density perturbations in GR. This relationship provides a useful means to derive constraints in terms of γ without compromising the precision of the calculation. Constraints on this quantity are presented in the $\gamma - \Omega_m$ plane in Figure 7. Gravitational lensing is not uniquely defined when using the γ parameter alone, so here we have simply set $\Sigma_0 = 0$ such that the lensing potential is unaltered from its conventional form. We find a value of $\gamma = 0.52 \pm 0.09$ for the case of a ΛCDM background. In Figure 8, we then let Σ_0 vary, presenting constraints in the $\gamma - \Sigma_0$ plane.

7.2 E_G **Parameter**

Proposed by Zhang et al. (2007), the E_G parameter encompasses contributions from both gravitational lensing and the motions of galaxies. This is in the form of a ratio which by construction nullifies contributions from both linear galaxy bias and the amplitude of
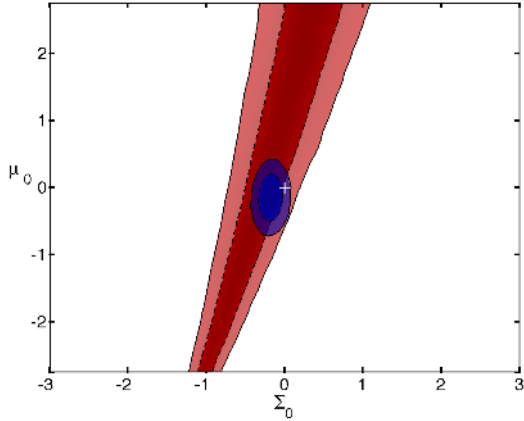
Figure 9. Confidence limits on the Σ_0 and μ_0 parameters derived from the measurement $E_G(z = 0.32) = 0.392 \pm 0.065$ (Reyes et al. 2010). The inner blue contours are the same as those in Figure 5. Here we assume a ΛCDM cosmology.

Figure 10. The same combinations of data as the left hand panel of Figure 5, except here we have replaced the Σ_0 parameter with the gravitational slip ζ_0 as defined in equation (19).

the matter power spectrum. The result is a quantity which is sensitive to both the lensing potential and the rate of structure formation

$$E_G \equiv \frac{\nabla^2 (\Phi + \Psi)}{3H_0^2 (1 + z)\beta\delta}, \tag{17}$$

where $\beta \equiv f/b$. This technique has been applied to SDSS data in Reyes et al. (2010). We cannot directly measure E_G with the CFHTLenS and WiggleZ datasets, since they do not overlap in sky coverage. However we can perform a direct mapping of the result from Reyes et al. (2010) onto the (μ, Σ) plane, utilising the relationship

$$E_G \simeq \frac{\Omega_m [1 + \Sigma(\bar{z})]}{f(\bar{z})}, \tag{18}$$

where the dependence on μ arises through its influence on $f(\bar{z})$, the linear growth rate at the mean redshift of the survey. The results are presented in Figure 9, where the red contours correspond to the confidence limits, in the $\mu_0 - \Sigma_0$ plane, arising from a combination of the measurement $E_G(z = 0.32) = 0.392 \pm 0.065$ (Reyes et al. 2010) with the BAO data from Section 3.2 which provide a constraint on Ω_m. The CMB does not provide further assistance in this case because the E_G parameter is insensitive to the amplitude of perturbations. For comparison, the inner blue contours match those in the right hand panel of Figure 5. We note that GR can readily generate departures from the conventional E_G value. For example in equation (18) the ratio $\Omega_m/f(\bar{z})$ changes when $\Omega_k \neq 0$ or $w \neq -1$. Similarly, radically different modified gravity models can generate an E_G value which appears consistent with the ΛCDM value. This is apparent from the degeneracy contour seen in Figure 9, where large values of both μ and Σ enhance the growth rate and lensing signal, leaving their ratio in equation (17) unchanged.

7.3 Gravitational Slip

Rather than modulating the sum of the two potentials using $\Sigma(a)$, it is often convenient to work in terms of the ratio of the potentials. One definition in this form is known as the gravitational slip ζ,
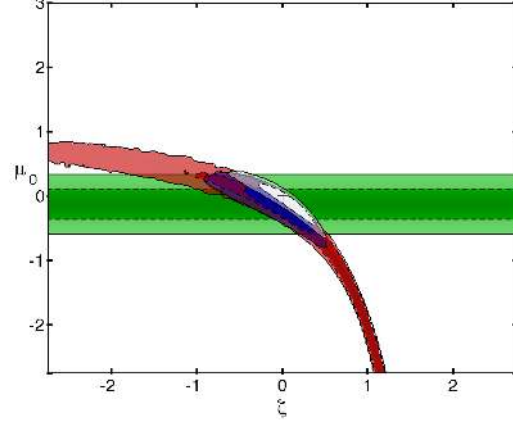
$$\zeta \equiv 1 - \frac{\Psi}{\Phi}, \tag{19}$$

which we expect to be zero in GR, in the absence of anisotropic stress. This has been the focus of much theoretical exploration, for example Ferreira & Skordis (2010) demonstrate that for second-order theories we generally expect to find this value scales with the Newtonian potential and its time derivative.

Recasting ζ in terms of (μ, Σ) using equations (4) and (5)

$$\zeta(a) = \frac{2 [\Sigma(a) - \mu(a)]}{1 + 2\Sigma(a) - \mu(a)}. \tag{20}$$

As an illustration in Figure 10 we reformulate the x-axis from Figure 5 in terms of ζ_0, the gravitational slip evaluated at $z = 0$. One striking feature of these contours are the long tails out to negative values of ζ and μ, corresponding to where the denominator Φ ventures close to zero. This suggests that the slip parameter may possess a pathological likelihood surface, and so for the purposes of performing Monte Carlo evaluations these contours are more safely generated as a derived parameter.

7.4 Gravitational Potentials

The redshift-space distortion data, used in this analysis, exhibits a peak sensitivity to a modified gravity scenario at approximately $z \simeq 0.5$ (see Section 8). In Figure 11 we therefore consider fractional deviations in the two gravitational potentials at this redshift, relative to their GR prediction for the same mass distribution. These are given by

$$\begin{aligned} \frac{\Delta\Psi}{\Psi} &= \mu(z), \\ \frac{\Delta\Phi}{\Phi} &= 2\Sigma(z) - \mu(z). \end{aligned} \tag{21}$$

where $\Delta\Psi \equiv \Psi - \Psi_{GR}$. For our conservative combined lensing, RSD, H_0 and high ℓ WMAP7 data analysis we find cosmological deviations in the Newtonian potential and curvature potential from the prediction of General Relativity to be $\Delta\Psi/\Psi = 0.05 \pm 0.25$ and $\Delta\Phi/\Phi = -0.05 \pm 0.3$ respectively (68 per cent CL).
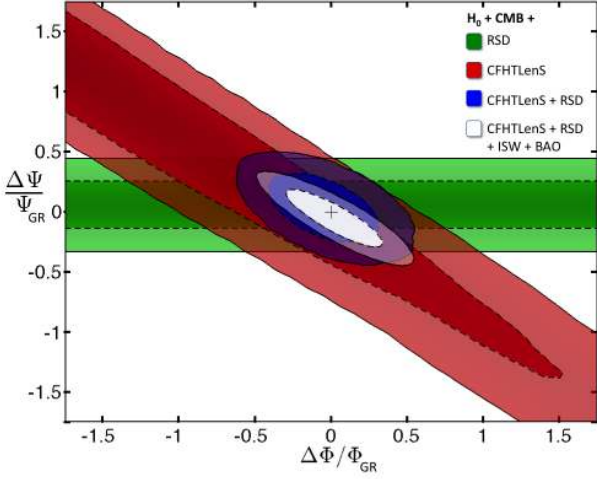
Figure 11. Here we explore fractional deviations in the two gravitational potentials, the Newtonian potential Ψ and the curvature potential Φ, from the GR value at $z = 0.5$. The prescription for this is given by equation (21). The contours represent the same combinations of data as those in the left hand panel of Figure 5.
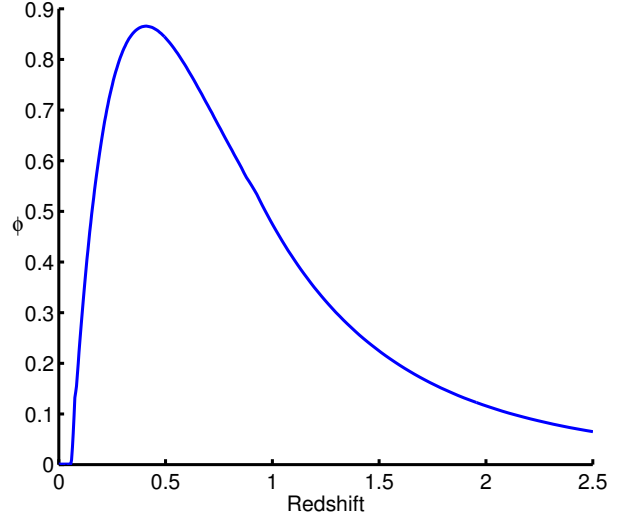
8   THEORETICAL MODELS

Below we briefly review some of the theoretical models which could generate a departure from $\mu_0 = \Sigma_0 = 0$, and interpret the implications of our results. There is such a plethora of modified gravity models, that no single choice of parameterisation can adequately encompass all of them. This is a situation reminiscent of the dark energy equation of state, $w(z)$, except here we are faced with uncertainty not only in the functional form of the time-dependence, but also in its scale-dependence. So how can we relate a given (μ, Σ) constraint to a specific model? The observed parameters $\hat{\mu}_0$ and $\hat{\Sigma}_0$ may be interpreted as a weighted integral over the true functional form $\mu(k, z)$, such that

$$\hat{\mu}_0 = \iint \phi(k, z)\, \mu(k, z)\, \frac{\Omega_\Lambda}{\Omega_\Lambda(z)}\, \mathrm{d}k\, \mathrm{d}z \,. \tag{22}$$

If we perform a scale- and time-dependent principal component analysis (see for example Zhao et al. 2009), then the weight function $\phi(k, z)$ may be expressed in terms of the principal components $e_i(k, z)$ and the errors associated with their corresponding eigenvalues $\sigma(\alpha_j)$ (Simpson & Bridle 2006), such that

$$\phi(k, z) = \frac{\sum_i e_i(k, z) \iint e_i(k', z') \mathrm{d}k'\, \mathrm{d}z' / \sigma^2(\alpha_i)}{\sum_j \left[\iint e_j(k'', z'') \mathrm{d}k''\, \mathrm{d}z''\right]^2 / \sigma^2(\alpha_j)} \,. \tag{23}$$

The analysis of redshift space distortions in Blake et al. (2012) includes information from the galaxy power spectrum up to a maximum wavenumber $k_{\max} = 0.2\, h\mathrm{Mpc}^{-1}$, corresponding to the regime over which the density and velocity fields are sufficiently linear for our theoretical models to remain valid. Since the number of Fourier modes increases towards higher k, the scale-dependent component of $\phi(k, z)$ peaks close to this value of $k_{\max}$, and $\phi(k, z) = 0$ for $k > k_{\max}$. We evaluate the redshift-dependence of the weight function $\phi(z)$ associated with the combined WiggleZ and 6dFGS data of Figure 3, following the prescription of Simpson & Bridle (2006), and this is shown to peak at $z \sim 0.5$ as illustrated in Figure 12. In the following subsections we utilise the weight function $\phi(z)$ presented in Figure 12 to map specific exam-

Figure 12. The redshift sensitivity of the modified gravity parameter μ_0. The weight function $\phi(z)$ is defined in equation (22) and evaluated with equation (23).

ples of theoretical models onto our parameter space, by evaluating equation (22). However as stressed earlier, we do not aim to place rigorous parameter constraints on any particular family of models.

8.1 $f(R)$

A more general form of the Einstein-Hilbert action replaces the Ricci scalar R with an arbitrary function $f(R)$ such that

$$S = \int f(R)\sqrt{-g}\, \mathrm{d}^4 x \,, \tag{24}$$

where g is the determinant of the metric tensor. This defines the broad class of $f(R)$ models. One of the most difficult tasks for any modified gravity model attempting to replace dark energy is to satisfy the stringent Solar System constraints, and most natural choices of the function $f(R)$ fail to do so. The subset of $f(R)$ models which have attracted interest are those which employ the so-called chameleon mechanism, where departures from GR are strongly suppressed in regions where R is large, only emerging when R is sufficiently small. Our location within the potential well of the Sun and the Milky Way halo may be sufficient to shield us from this unusual gravitational behaviour.

For a particular subset of $f(R)$ models which are capable of satisfying Solar System tests, the departure from GR may be characterised as (Zhao et al. 2012)

$$\mu(k, a) = \frac{1}{3 + 3(aM/k)^2} \,, \tag{25}$$

where the scalaron mass $M(a) = 1/\sqrt{3\, \mathrm{d}^2 f/\mathrm{d}R^2}$. For any given redshift and wavenumber, the value of μ lies in the range $0 \leqslant \mu < \frac{1}{3}$. This generically enhances growth, so we expect this family of models to lie vertically above the point $(0, 0)$ in Figure 5. We parameterise $M = M_0 a^{-\sigma}$ and take as an example $M_0 = 0.02\, h\mathrm{Mpc}^{-1}$ and $\sigma = 3$, corresponding to the type of model explored in Zhao et al. (2012). In $f(R)$ models the lensing potential for a given mass distribution is unchanged from the case of GR, and so $\Sigma_0^{f(R)} = 0$. Our measure of μ is dominated by the

RSD data and by evaluating equation (22) this model ought to map onto our (μ, Σ) plane at a value of $\mu_0^{f(R)} = 0.81$. This is despite $\mu(a)$ never rising above $1/3$, but the stronger deviation from GR at high redshift compared to our parameterisation allows a higher effective value of μ_0 to be generated. Our data therefore disfavour the more aggressive $f(R)$ models, in agreement with the findings of Zhao et al. (2012).

8.2 DGP

The higher-dimensional model proposed by Dvali, Gabadadze, & Porrati (2000) has proved one of the most popular gravitational models for theoretical and experimental exploration. It is of particular interest due to its physical motivation and specific observational prediction, namely a value of the growth index $\gamma = \frac{11}{16}$, or equivalently $\mu_0 = -\frac{25}{48}\Omega_\Lambda; \Sigma_0 = 0$. However in its most natural form there appears significant disparity with observational data (see for example Lombriser et al. 2009). This can be bypassed by introducing a cosmological constant, although this somewhat compromises the motivation of the DGP model.

In general the behaviour of DGP is a scale-independent suppression of the growth of structure. Like $f(R)$, the lensing potential is unaltered so $\Sigma_0^{\mathrm{DGP}} = 0$. Adopting a fiducial value $\Omega_\Lambda = 0.27$ leaves us with $\mu_0^{\mathrm{DGP}} = -0.38$. This negative value of μ remains consistent with our data.

8.3 Newtonian Limit

The point at $\mu_0 = 0; \Sigma_0 = -0.5$ corresponds to a scenario where the present-day cosmological gravity resembles Newtonian gravity. That is, the angular deflection of light is half the value predicted by Einstein at $z = 0$, while the forces experienced by galaxies remain unchanged. This model was famously rejected in favour of General Relativity by Dyson et al. (1920). The difference here is that we are performing this test on cosmological scales. Whether we combine our gravitational data with either BAO or the H_0 prior, the results are the same, a value of $\Sigma_0 = -0.5$ is strongly disfavoured by the data.

Another regime of interest is that of $\mu_0 < -1$, for this corresponds to the anti-gravitational behaviour of galaxies, in that they are repulsed from clusters and attracted towards voids. One might naively expect that if dark energy is gravitational in origin, then the repulsive nature of the expansion may also be seen within the perturbations. This region is disfavoured by the data when assuming a flat ΛCDM background, but this is no longer the case for more general backgrounds since the regime $w < -1$ permits more negative values of μ_0, as seen in the central panel of Figure 6.

8.4 Interacting Dark Energy

When conducting cosmological tests of gravity, in this work and in others (Daniel et al. 2010; Bean & Tangmatitham 2010; Zhao et al. 2010; Song et al. 2011; Reyes et al. 2010; Tereno et al. 2011; Zuntz et al. 2012; Zhao et al. 2012; Rapetti et al. 2012), we necessarily make certain assumptions such as the lack of anisotropic stress. One assumption not often made explicit is that dark energy exhibits negligible interactions with dark matter, aside from their mutual gravitational repulsion. If the two fluids were to exchange energy and momentum, this readily alters the growth of structure (Amendola 2000; Simpson et al. 2011; Simpson 2010), and so could generate a false signature of modified gravity.

In the simplest interacting models, we would expect to see an alteration in the growth of large scale structure, but no direct change to the lensing potential. Thus detecting a non-zero value of Σ_0 is a prerequisite for confirming a truly modified gravity scenario. That is to say, we cannot perform a cosmological test of gravity without gravitational lensing.

As an illustrative example, we consider the scenario of dark energy decaying into a form of dark matter. If this results in the dark matter density following a power law $\rho = \rho_0 a^{-3+\epsilon}$, the growth rate of cosmic structure is subject to a constant decrement (Simpson et al. 2011)

$$f(a) = \Omega_m^\gamma(a) - \frac{67}{55}\epsilon. \qquad (26)$$

Large values of ϵ lead to a significant quantity of dark energy in the early Universe, and as such are disfavoured by observations of the CMB. Taking $\epsilon = 0.01$, which is small enough not to perturb the primary anisotropies of the CMB, leads to an effective value $\mu_0^\epsilon = -0.99$ and $\Sigma_0^\epsilon = 0$, a region which is disfavored by our results.

9 CONCLUSIONS

In this work we find no indication of a departure from General Relativity on cosmological scales, having explored the behaviour of non-relativistic and relativistic particles in the WiggleZ, 6dFGS, and CFHTLenS data. Both the motions of galaxies and the deflection of their emitted light conform to the predictions of Einstein's theory, at the level of precision permitted by current data. We place limits on our gravitational parameters $\mu_0 = 0.05 \pm 0.25$ and $\Sigma_0 = 0.00 \pm 0.14$ for a flat ΛCDM expansion history. This corresponds to deviations in the present-day time dilation and spatial curvature of $\Delta\Psi/\Psi_{\mathrm{GR}} = 0.05 \pm 0.25$ and $\Delta\Phi/\Phi_{\mathrm{GR}} = -0.05 \pm 0.3$ respectively. However these errors are significantly correlated, as shown in Figure 11.

For ground-based and solar system tests, where light-travel time is short, it is relatively straightforward to conduct a geometric measurement. Cosmological experiments do not share this luxury, and considerable effort is required in order to determine the spatial positioning of the test subjects. The precision at which we map the geometry of the Universe remains one of the limiting factors in determining its gravitational potentials. This is particularly apparent when increased freedom in the cosmic expansion history is allowed, arising from a variable dark energy equation of state or nonzero global curvature. Further geometric data could be included in the analysis, such as those derived from the light curves of Type Ia supernovae. However combining a large number of datasets leaves us increasingly exposed to the effects of systematic errors. For the purposes of gravitational lensing, another source of uncertainty is the form of the matter power spectrum on nonlinear scales, and this is an issue which will likely become more acute with the advent of surveys spanning a large fraction of the sky. Higher resolution N-body simulations can help to a certain extent, but modelling the influence of baryons may prove particularly problematic.

The absence of a compelling theoretical rival to GR makes a suitable choice of gravitational parameters rather uncertain. In order to minimise the number of degrees of freedom, and to maintain sensitivity to a broad range of models, we adopted a scale-independent modification to the Newtonian and curvature potentials. The scale-dependence of our results is implicit in the wide range of sensitivities each probe possesses. The cosmic shear signal

from CFHTLenS is sourced by density perturbations of the order $\sim 5\, h^{-1}\mathrm{Mpc}$, while the redshift space distortions from WiggleZ involve Fourier modes with wavelengths over $30\, h^{-1}\mathrm{Mpc}$. Furthermore the ISW effect causes the largest angular scales of the CMB to receive significant contributions from gravitational perturbations in excess of $\sim 500\, h^{-1}\mathrm{Mpc}$. If any inconsistency were seen between these results this could have been an indication of scale-dependent behaviour. Our reasons for focussing on a time dependent variation that mimics the dominance of dark energy rather than using constant μ and Σ values are twofold. First our motivation for seeking modification to General Relativity stems from dark energy, a phenomenon which only appears at late times. Furthermore, if we were to investigate constant μ and Σ parameters, our constraints would be dominated by the primary anisotropies of the cosmic microwave background, which as shown in previous studies (Bean & Tangmatitham 2010; Zuntz et al. 2012) is consistent with a GR framework.

Solar system experiments have already eliminated many potential modifications to GR which could have provided a natural explanation for the accelerating Universe. Here we have begun to disfavour some of those which remain. While the volume of parameter space available to modified gravity models continues to shrink, the cosmological constant retains its position as the most viable solution to the dark energy problem.

APPENDIX A: TREATMENT OF THE CMB

In our analysis we use the $\ell \geqslant 100$ WMAP7 data from the C_ℓ^{TT} and C_ℓ^{TE} power spectra to constrain geometric cosmological parameters, as well as a benchmark for the amplitude of matter perturbations. In contrast, the $\ell < 100$ multipoles provide additional information on the gravitational potentials through the ISW. Discarding the low multipoles would severely compromise our ability to constrain the primordial amplitude of density perturbations. This is because on small angular scales there is a strong degeneracy between the optical depth τ and the amplitude A_s, since both parameters induce a simple scaling of the amplitude. To circumvent this problem we first run a likelihood analysis on the low multipoles $2 \leqslant \ell < 100$, marginalising over our full parameter set including μ_0 and Σ_0. This establishes a prior on τ, which we then use in our analysis of the data, except in those cases where the low multipoles are included. Despite the addition of modified gravity parameters, we find little degradation in the constraint on τ compared to the standard WMAP7 result which assumes GR. This is due to the unique signature left by τ at the large scales of the C_ℓ^{TE} spectrum, which cannot be replicated by the other parameters.

To illustrate the impact of removing the WMAP7 data, we present in Figure A1 the results for CFHTLenS $+H_0$ in red, and
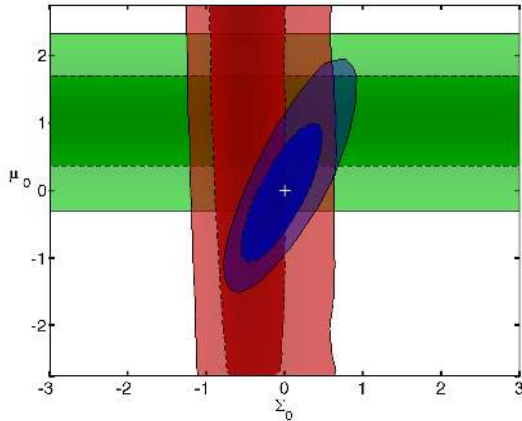
Figure A1. Constraints on our modified gravity parameters μ_0 and Σ_0 from redshift space distortions (green), weak lensing (red), and combined (blue), for a flat ΛCDM background. A prior on H_0 is included, but there is no additional information from the CMB. The dashed contours represent the 68 and 95 per cent confidence intervals, while the cross denotes the prediction of GR.

WiggleZ $+H_0$ in green. The substantial degradation in these contours highlights the importance of including the high$-\ell$ data.

REFERENCES

Alcock C., Paczynski B., 1979, Nature , 281, 358
Amendola L., 2000, PRD , 62, 043511
Amendola L., Kunz M., Sapone D., 2008, JCAP, 4, 13
Anderson L. et al., 2012, ArXiv e-prints: 1203.6594
Ballinger W. E., Peacock J. A., Heavens A. F., 1996, MNRAS , 282, 877
Bartelmann M., Schneider P., 2001, Phys. Rep. , 340, 291
Bean R., Tangmatitham M., 2010, PRD , 81, 083534
Benjamin J. et al., 2012, MNRAS submitted
Bertotti B., Iess L., Tortora P., 2003, Nature , 425, 374
Bertschinger E., 2006, ApJ , 648, 797
Beutler F. et al., 2011, MNRAS , 416, 3017
Beutler F. et al., 2012, MNRAS , 423, 3430
Blake C. et al., 2012, MNRAS , 425, 405
Blake C. et al., 2011, MNRAS , 415, 2876
Clifton T., Ferreira P. G., Padilla A., Skordis C., 2012, Phys. Rep. , 513, 1
Daniel S. F., Linder E. V., Smith T. L., Caldwell R. R., Cooray A., Leauthaud A., Lombriser L., 2010, PRD , 81, 123508
Doré O. et al., 2007, ArXiv e-prints: 0712.1599
Drinkwater M. J. et al., 2010, MNRAS , 401, 1429
Dvali G., Gabadadze G., Porrati M., 2000, Physics Letters B, 485, 208
Dyson F. W., Eddington A. S., Davidson C., 1920, Royal Society of London Philosophical Transactions Series A, 220, 291
Einstein A., 1916, Annalen der Physik, 354, 769
Eisenstein D. J., Hu W., 1998, ApJ , 496, 605
Erben T. et al., 2009, A&A , 493, 1197
Ferreira P. G., Skordis C., 2010, PRD , 81, 104020
Gilbank D. G., Gladders M. D., Yee H. K. C., Hsieh B. C., 2011, AJ , 141, 94
Guzzo L. et al., 2008, Nature , 451, 541

Harnois-Déraps J., Vafaei S., Van Waerbeke L., 2012, MNRAS , 426, 1262
Hawkins E. et al., 2003, MNRAS , 346, 78
Heymans C. et al., 2012, MNRAS , 427, 146
Heymans C., White M., Heavens A., Vale C., van Waerbeke L., 2006, MNRAS , 371, 750
Hildebrandt H. et al., 2012, MNRAS , 421, 2355
Hojjati A., Pogosian L., Zhao G.-B., 2011, JCAP, 8, 5
Hudson M. J., Turnbull S. J., 2012, ApJL , 751, L30
Jain B., Vikram V., Sakstein J., 2012, ArXiv e-prints: 1204.6044
Jennings E., Baugh C. M., Pascoli S., 2011, MNRAS , 410, 2081
Joachimi B., Mandelbaum R., Abdalla F. B., Bridle S. L., 2011, A&A , 527, A26
Jones D. H. et al., 2009, MNRAS , 399, 683
Jones D. H. et al., 2004, MNRAS , 355, 747
Kaiser N., 1987, MNRAS , 227, 1
Kilbinger M., Benabed K., Cappe O., Cardoso J.-F., Fort G., Prunet S., Robert C. P., Wraith D., 2011, ArXiv e-prints: 1101.0950
Kilbinger M. et al., 2012, MNRAS submitted
Komatsu E., Seljak U., 2002, MNRAS , 336, 1256
Komatsu E. et al., 2011, ApJS , 192, 18
Larson D. et al., 2011, ApJS , 192, 16
Lewis A., Challinor A., Lasenby A., 2000, ApJ , 538, 473
Linder E. V., 2005, PRD , 72, 043529
Linder E. V., Cahn R. N., 2007, Astroparticle Physics, 28, 481
Lombriser L., Hu W., Fang W., Seljak U., 2009, PRD , 80, 063536
Martin D. C. et al., 2005, ApJL , 619, L1
Matsubara T., Suto Y., 1996, ApJL , 470, L1+
McDonald P., Trac H., Contaldi C., 2006, MNRAS , 366, 547
Mehta K. T., Cuesta A. J., Xu X., Eisenstein D. J., Padmanabhan N., 2012, ArXiv e-prints: 1202.0092
Miller L. et al., 2012, MNRAS accepted
Padmanabhan N., Xu X., Eisenstein D. J., Scalzo R., Cuesta A. J., Mehta K. T., Kazin E., 2012, ArXiv e-prints: 1202.0090
Peacock J. A. et al., 2001, Nature , 410, 169
Rapetti D., Blake C., Allen S. W., Mantz A., Parkinson D., Beutler F., 2012, ArXiv e-prints: 1205.4679
Reid B. A. et al., 2012, MNRAS , 426, 2719
Reyes R., Mandelbaum R., Seljak U., Baldauf T., Gunn J. E., Lombriser L., Smith R. E., 2010, Nature , 464, 256
Riess A. G. et al., 2011, ApJ , 730, 119
Samushia L. et al., 2012, ArXiv e-prints: 1206.5309
Schrabback T. et al., 2010, A&A , 516, A63
Semboloni E., Hoekstra H., Schaye J., van Daalen M. P., McCarthy I. G., 2011, MNRAS , 417, 2020
Seo H.-J., Eisenstein D. J., 2003, ApJ , 598, 720
Sharp R. et al., 2006, in Society of Photo-Optical Instrumentation Engineers (SPIE) Conference Series, Vol. 6269, Society of Photo-Optical Instrumentation Engineers (SPIE) Conference Series
Simpson F., 2010, PRD , 82, 083505
Simpson F., Bridle S., 2006, PRD , 73, 083001
Simpson F., Jackson B., Peacock J. A., 2011, MNRAS , 411, 1053
Simpson F., Peacock J. A., 2010, PRD , 81, 043512
Smith R. E. et al., 2003, MNRAS , 341, 1311
Song Y.-S., Zhao G.-B., Bacon D., Koyama K., Nichol R. C., Pogosian L., 2011, PRD , 84, 083523
Spergel D. N. et al., 2007, ApJS , 170, 377
Tereno I., Semboloni E., Schrabback T., 2011, A&A , 530, A68
Wang L., Steinhardt P. J., 1998, ApJ , 508, 483
White M., Kochanek C. S., 2001, ApJ , 560, 539
York D. G. et al., 2000, AJ , 120, 1579

Zhang P., Liguori M., Bean R., Dodelson S., 2007, Physical Review Letters, 99, 141302

Zhao G.-B., Giannantonio T., Pogosian L., Silvestri A., Bacon D. J., Koyama K., Nichol R. C., Song Y.-S., 2010, PRD , 81, 103510

Zhao G.-B., Li H., Linder E. V., Koyama K., Bacon D. J., Zhang X., 2012, PRD , 85, 123546

Zhao G.-B., Pogosian L., Silvestri A., Zylberberg J., 2009, Physical Review Letters, 103, 241301

Zuntz J., Baker T., Ferreira P. G., Skordis C., 2012, JCAP, 6, 32